In-Situ Synthesis of Reduced Graphene Oxide/Aluminium Oxide Nanopowders for Reinforcing Ti-6Al-4V Composites

H. Xue [a], M. Zhu [a**], L.L. Dong [b, c*], W. Zhang [b], X.C. Sun[d], Y.M. Wang [a], Y.Q. Fu [e], Y.S. Zhang [f]

[a] School of Materials Science and Engineering, Xi'an University of Science and Technology, Xi'an, 710054, P.R. China

[b] Advanced Materials Research Central, Northwest Institute for Nonferrous Metal Research, Xi'an 710016, P.R. China

[c] School of Materials Science and Engineering, Northeastern University, Shenyang 110819, P.R. China

[d] Shandong Nanshan Institute of Science and Technology, Yantai, 265700, P.R. China

[e] Faculty of Engineering and Environment, Northumbria University, Newcastle upon Tyne NE1 8ST, UK

[f] Xi'an Rare Metal Materials Institute Co., Ltd. Xi'an 710016, P.R. China

ABSTRACT:

Carbon nanomaterials (such as graphene, carbon nanotubes and nano-diamond) are widely used to synthesize metal matrix composites to strengthen metals such as Ti, Al and Cu. However, severe aggregation of these nano-scale reinforcements within the metal

[*]Corresponding author:

E-mail address: donglong1027@163.com, mingzhu@xust.edu.cn

matrix has been a serious issue to achieve good performance metal matrix composites. In this study, we employed an *in-situ* co-precipitation method to decorate reduced graphene oxides with aluminium oxide nanoparticles (i.e. rGONs@Al_2O_3), which were then introduced into Ti-6Al-4V matrix using the processes of ball milling and spark plasma sintering. Effects of co-precipitation temperature on the characteristics of rGONs/Al_2O_3 nanopowders, and their concentrations on microstructures and mechanical properties of the composites were systemically investigated. Characterization results revealed that γ-Al_2O_3 nanoparticles were uniformly wrapped with rGONs fakes, and numbers and sizes of Al_2O_3 nanoparticles were decreased with the increase of co-precipitation temperature. The rGONs@Al_2O_3 nanoparticles were uniformly coated onto the surfaces of the Ti-6Al-4V powders, thus achieving a much finer grain size of matrix after the sintering process. As the content of rGONs@Al_2O_3 was increased, the strength of the composites was enhanced, whereas the elongation was slightly decreased. Due to effects of grain refinement and effective load transfer, the composite of 0.5 wt% rGONs@Al_2O_3 has achieved a high yield strength and an ultimate tensile strength of 950 MPa and 1022 MPa, which were ~120.4% and ~117.1% of the TC4 matrix, respectively. The fracture morphology was a mixture of cleavage fracture and ductile fracture.

KEYWORDS: Ti matrix composites, rGONs@Al_2O_3 nanopowders, Spark plasma sintering, Mechanical properties, *In-situ* reaction

1. Introduction

Titanium and its alloys are widely used in aerospace, biomedicine and automobile fields [1, 2]. However, their applications are often limited owing to their poor mechanical properties under severe working conditions. Therefore, titanium matrix composites (TiMCs) have been extensively studied owing to their light weight, high specific strength, and excellent corrosion resistance [3-5]. To further enhance the mechanical properties of TiMCs, many ceramics particles with high hardness and modulus, such as TiB, TiC, ZrO_2, Al_2O_3 and Y_2O_3, have been applied as the reinforcements of the TiMCs [6-9]. For example, Shen et al [10] found that TiB/Ti composites enhanced with 15 wt.% TiB_2 fabricated by spark plasma sintering (SPS) exhibited a relative density of 99.6% and a bending strength of 1161 MPa.

Attributed to their superior mechanical and physical properties [11-13], graphene and its derivatives were frequently chosen as the new types of reinforcements to fabricate TiMCs with superior strength and good ductility [14]. Some of the collected data published in literature are listed in **Table 1**. For example, Yan et al [15] fabricated graphene/TC4 composites with a quasi-networked microstructure using a high energy ball milling followed by the SPS, and they reported that the strength and hardness were increased up to ~126% and ~114.6% compared with those of Ti–6Al–4V (TC4) matrix. Previously, we reported that the GONs-*x*Cu/TC4 composites prepared by a two-step process including ball milling and SPS exhibited high hardness and good tribological properties [16]. However, graphene often shows its poor dispersion capability in a metal

matrix due to its strong Van der Waals force, thus its strengthening effect was often not as good as expected [17]. Hence, many methods including high energy ball milling [18], three-dimensional dynamic mixing [19], ultrasonic stirring [20], electrostatic adsorption [21] and surfactants [22] were applied to improve the dispersion of graphene in the metal matrix.

Table 1. Comparisons of effects of graphene reinforcements in Ti matrix reported in literature.

Reinforcement/matrix	Contents	Dispersion methods	Preparation process	Yield strength/MPa	Tensile strength/MPa	Elongation /%	Ref.
rGO/TC4	0.6%wt GONs	Stirring	SPS (45MPa, 100°C/min, 1000°C for 5min)	446	535	6.0	[20]
GR/Ti	0.25%wt GR	Surfactant-PVA Stirring	SPS (60MPa, 50°C/min, 700°C for 10min, 1000°C for 5min)	940	968	10.0	[22]
	0.5%wt GR			938	940	4.3	
	0.5%wt GR			892	892	3.6	
GONs/Ti	0.3%wt GONs	Stirring	SPS (45MPa, 100°C/min 1100°C for 5min)	433	545	22.9	[23]
	0.6%wt GONs			410	534	20.5	
	0.9%wt GONs			419	541	20.1	
GNPs, GONs, GPs/TC4	0.15%wt GNPs	Ultrasonic, stirring and ball milling	SPS (45MPa, 100°C/min 900 °C for 5min)	942	980	1.8	[14]
	0.15%wt GONs			898	951	5.4	
	0.15%wt GPs			836	963	3	
GNPs/TC21	0.05%wt GNPs	Ball milling	SPS (45MPa, 100°C/min 1000 °C for 5min)	1017	1162	13.2	[24]
	0.1%wt GNPs			1001	1146	10.6	
	0.3%wt GNPs			998	1135.4	9.1	
MLG/Ti	0.5%wt MLG	Dispersant-SDBS and ball milling	SPS (40MPa, 150C/min 1100 °C for 6min)	918	-	-	[25]
	1.5%wt MLG			800	-	-	

	0.1%wt MLG		SPS (500MPa,	897	977	11.7	
MLG/TC4	0.15%wt MLG	3D dynamic mixing	50^{o}C/min	938	1010	9.0	[26]
	0.2%wt MLG		700^{o}C for 10min)	949	1005	3.8	
			SPS (30MPa,				
GNSs/TC4	0.5%wt GNSs	Rocking mixing,	50^{o}C/min	947	1013	3.6	[15]
			1100^{o}C for 10min)				
	0.05%wt GNPs	Ultrasonic,	SPS (60MPa,	924	986	17.4	
GNPs/CT20	0.1%wt GNPs	stirring and	50^{o}C/min	836	917	20	[27]
	0.15%wt GNPs	ball milling	1000^{o}C for 6min)	760	820	21.5	

PVA= Polyvinyl alcohol, SDBS= Sodium dodecyl-benzene sulphonate rGO= Reduced graphene oxide, GR= Graphene, MLG=Multilayer graphene, GNPs=Graphene nanoplates, GONs= Graphene oxides nanosheets, GPs= Graphite powders, GNSs= Graphene nanosheets

Currently, many researchers are focusing on modifying the surfaces of graphene-based nanomaterials with various types of nanoparticles/nanolayers (such as Ag [28, 29], Cu [30], Au [31], Pt [32], Ni [33], Al_2O_3 [34], tungsten carbide [35]). The aims are to prevent graphene from agglomeration and enhance the functional, physical and mechanical properties of the composites. Recently we reported that a good balance of strength and ductility (e.g., 846 MPa-11.6% for the Cu@rGO/Ti composites and 900 MPa-8.4% for the Ag@rGO/Ti composites, respectively) was achieved in a Ti matrix composite using reinforcement nanopowders, which were formed by reduced graphene oxide nanosheets decorated with copper or silver (i.e. Cu@rGO and Ag@rGO) [36]. Furthermore, Cu matrix was reinforced using 0.6 vol% Ag@rGO nanoparticles, and the composites showed 98% and 93% enhancements in 0.2% yield strength and ultimate tensile strength, respectively, as compared to those of pure Cu [28]. Fu et al [37] fabricated 1.0 wt% Ni@graphene/Ni composites using processes of *in-situ* high-temperature chemical vapor deposition process and SPS, and their results showed 188.4% and 26.0% enhancements in 0.2% yield strength and ultimate tensile strength, respectively, compared with those of pure Ni matrix. However, the elongation of the composites was decreased (from 36.7% to 25.5%). Guan et al [38] reported that with the increase of Ni-coated GNSs contents, the strength of Ni-coated GNSs/Al composites increased, and the elongation of the composites was decreased from 20.3% to 8.7%, which is a reduction of 57.1%. Shuai et al [39] synthesized the MgO@rGO powders using an *in-situ* synthesis method, and then used these powders to synthesize AZ61

magnesium alloy-based composites using a laser melting method. Their results showed that not only the corrosion resistance of the MgO@rGO/AZ61 composites was improved, but also their compressive strength and hardness were increased up to 241.2 MPa (+10%) and 108 HV (+8%). All the above studies show that carbon nanomaterials modified with ceramic nanoparticles could be effectively applied in strengthening metal matrix composites. However, Ti matrix based nanocomposites using a powder metallurgy route have seldomly been reported so far, and the microstructure and mechanical properties of such composites have not been reported.

Herein, reduced graphene oxides decorated with aluminium oxide nanoparticles (i.e. the rGONs@Al_2O_3 nanopowders) were synthesized using an *in-situ* co-precipitation method, followed by a high temperature calcination at 400 °C for 2 hours in a vacuum chamber. Effects of co-precipitation process temperature on morphology, phases, chemical composition and formation mechanism of the rGONs/Al_2O_3 nanopowders were investigated.

Figure 1(a) illustrates the mechanism of deposition Al_2O_3 particles on the surface of rGONs using our developed technology. GONs nanomaterials have negatively charged ions and excellent dispersibility in the aqueous environment due to many functional-oxygen groups (i.e. -COOH, -OH etc.) at their edges **(I)** [40]. When aluminum chloride solution is added into the GONs dispersion, Al^{3+} ions are absorbed on the surface of the GONs due to the electrostatic attraction **(II)**. Al^{3+} ions are turned into aluminum hydroxide colloid after the addition of sodium hydroxide **(III)**. Finally, a large number of

small molecules such as H_2O, CO_2, and O_2 in the composites are eliminated during the calcination process **(V)** [41]. As a result, the GONs were mostly reduced into rGONs after the calcination, and Al_2O_3 particles are bound onto the rGONs through *in-situ* nucleation and growth. The reactions described above can be expressed by the following two equations:

$$GO+AlCl_3\cdot 6H_2O+NaOH \xrightarrow{\Delta} G\text{-}O\text{-}Al(OH)_3+NaCl+H_2O \qquad (1)$$

$$G\text{-}O\text{-}Al(OH)_3 \xrightarrow{400^{\circ}C\ 2h} RGO\text{-}Al_2O_3+CO_2\uparrow+H_2O\uparrow \qquad (2)$$

Composites of rGONs@Al_2O_3/TC4 are then fabricated using these powders and Ti-6Al-4V (TC4) powders and a low-energy ball milling process followed by a SPS process. **Figure 1(b)** illustrates the microstructure of the nanocomposites, in which powders of rGONs@Al_2O_3 (also rGONs and Al_2O_3) are uniformly distributed inside a matrix of TC4. **Figure1 (b)** also shows the crack propagation in the rGONs@Al_2O_3/TC4 composites. The cracks easily generate at the interfaces of the Al_2O_3/rGONs/TC4, and they could have two major modes of crack propagations, e.g., (1) through boundaries between Al_2O_3 particles and rGONs; (2) cutting through Al_2O_3 particles and rGONs, as illustrated in **Figure 1(b)**. However, both these two crack propagation routes require more energy to be absorbed, thus the strength of composites is improved dramatically.

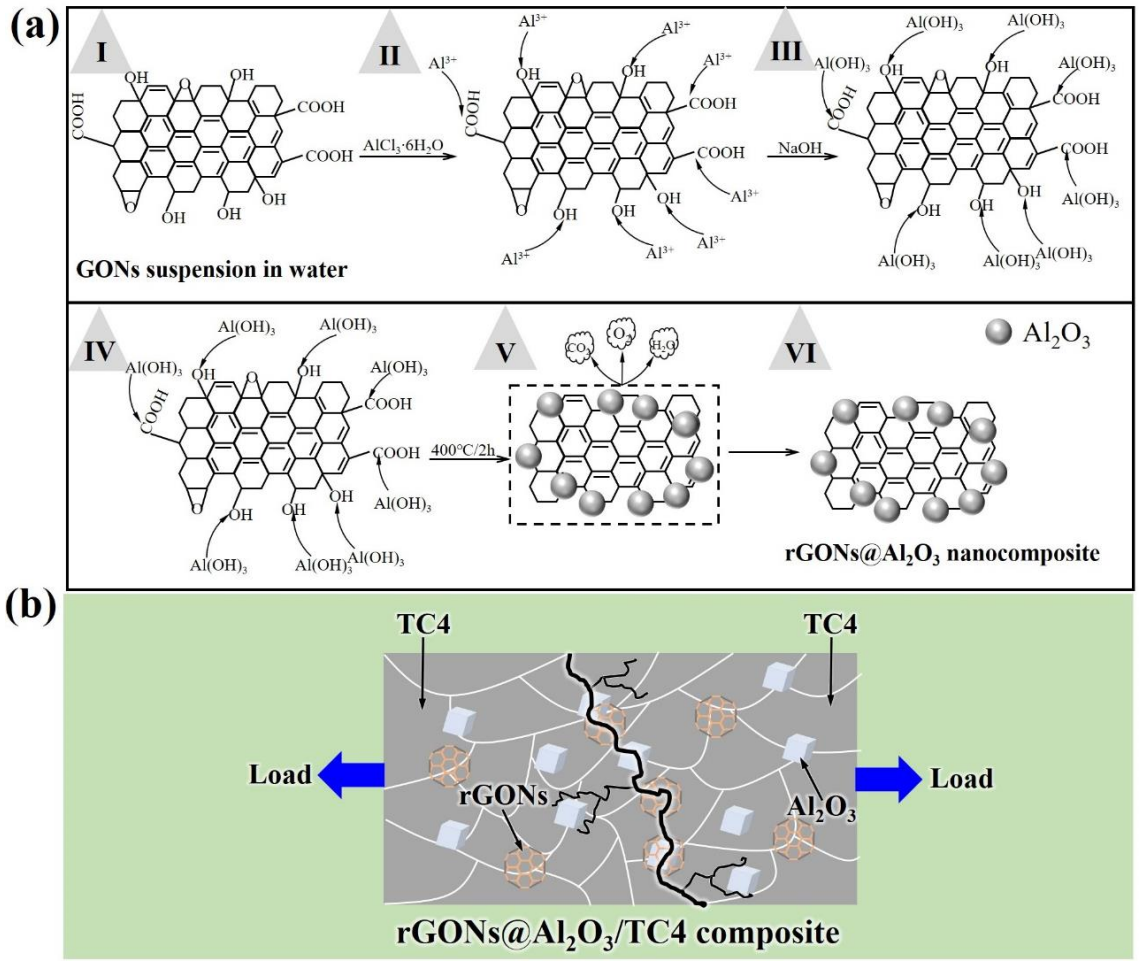

Figure 1. (a) Illustrations of formation mechanism for the designed rGONs@Al_2O_3 nanocomposite; and (b) Schematic illustration of microstructure of rGONs@Al_2O_3/TC4 nanocomposites, and crack propagation inside the composites.

2. Material and methods

2.1 Raw materials

Graphene oxide nanosheets (GONs, with a thickness of 1-3 nm and a diameter of 0.5-5 μm) were purchased from Nanjing Xian-Feng Nano Materials Technology Co. Ltd., China. Transmission electron microscope (TEM) image shown in **Figure 2(a)** revealed

that the GONs have large-scale, transparent, and folded structures. Select electron diffraction pattern of the GONs (inset in **Figure 1a**) confirms the low degree of crystallinity GONs. However, there are many nanoscale defects at the boundary of GONs, as marked by white arrows shown in **Figure 2(b)**, which could facilitate the easy *in-situ* deposition of Al_2O_3 nanoparticles onto the surfaces of GONs. Commercially available Ti–6Al–4V powders with an average size of 15~53 μm were purchased from Xi'an SinoEuro Materials Technologies Co., Ltd., China. Aluminum chloride hexahydrate (of an analytical grade) was purchased from Sinopharm Chemical Reagent Co., Ltd., China, and sodium hydroxide (analytical grade) was purchased from Tianjin Zhiyuan Chemical Reagent Co., Ltd, China.

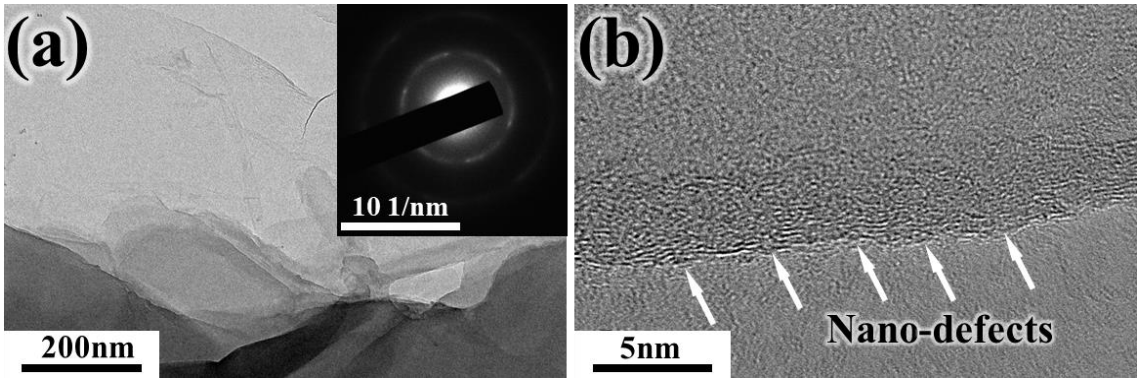

Figure 2. (a) TEM image (inset shows the select electron diffraction pattern) and (b) high resolution TEM images of GONs.

2.2 Fabrication of rGONs@Al_2O_3/TC4 composites

In order to improve the dispersion of graphene nanomaterials into TC4 powders, the rGONs@Al_2O_3 nanopowders were synthesized using an *in-situ* chemical co-precipitation

method combined with a calcination process, as illustrated in **Figure 3** (the stage 1). The detailed synthesis processes of the stage 1 are listed as follows.

(1) 0.3 g of GONs were uniformly dispersed into 500 ml deionized water with the help of ultrasonic and mechanical stirring for 180 min;

(2) 500 ml of aluminum chloride (0.0075 g/ml) was added into the above dispersion of GONs drop by drop, and stirred at different temperatures (i.e., 60, 80 and 90 ^{o}C) for 240 min;

(3) 500 ml of sodium hydroxide solution (0.006 g/ml) was added into the above solution under a continuous stirring for 12 h;

(4) To obtain rGONs@Al_2O_3 nanocomposite powders, the obtained solution was centrifugally washed with deionized water for three times, freeze dried for 48 h and calcined at 400 °C in a vacuum chamber for 2 h. The rGONs@Al_2O_3 nanocomposite powders prepared at different chemical co-precipitation temperatures were named as 60-rGONs@Al_2O_3, 80-rGONs@Al_2O_3 and 90-rGONs@Al_2O_3 for the easy identifications. To determine the phase contents of rGONs@Al_2O_3 powders, the thermogravimetric analysis tests were conducted in the ambient atmosphere but at different temperatures from 25^{o}C to 1000^{o}C (shown in **Figure S1**). **Figure S1** also displays the weight loss curve of 60-rGONs@Al_2O_3 nanopowders and the sample had a total weight loss of 21.6 wt%. No weight loss can be observed above 600 °C, revealing that the residual substance residue is Al_2O_3. Therefore, we can confirm that the rGONs@Al_2O_3 nanopowders are

composed of 21.6% rGONs and 78.4% Al_2O_3. **Figure 3** shows the stage 2 of the process for the powder metallurgy synthesis process of the rGONs@Al_2O_3/TC4 composites.

(5) As-received rGONs@Al_2O_3 nanopowders and TC4 powders were put into stainless steel jar containing stainless steel balls with three different diameters (8, 5 and 2 mm, and their weight ratio of 3:2:1) and were milled at a speed of 200 rpm for 8 h. The weight ratio of ball to powder was 3:1.

(6) To obtain the rGONs@Al_2O_3/TC4 composites, the mixed powders were transferred into a graphite mould with an internal diameter of 50 mm. They were densified using the SPS at 1000^{o}C for 5 min under a pressure of 45 MPa in vacuum, with a heating rate of 100^{o}C/min. The TC4 composites with two different contents of rGONs@Al_2O_3 (i.e., 0.3wt% and 0.5wt%) were finally prepared. For comparisons, rGONs/TC4 composites were also prepared using a hydrothermal stirring synthesis method, with the same sintering process as above.

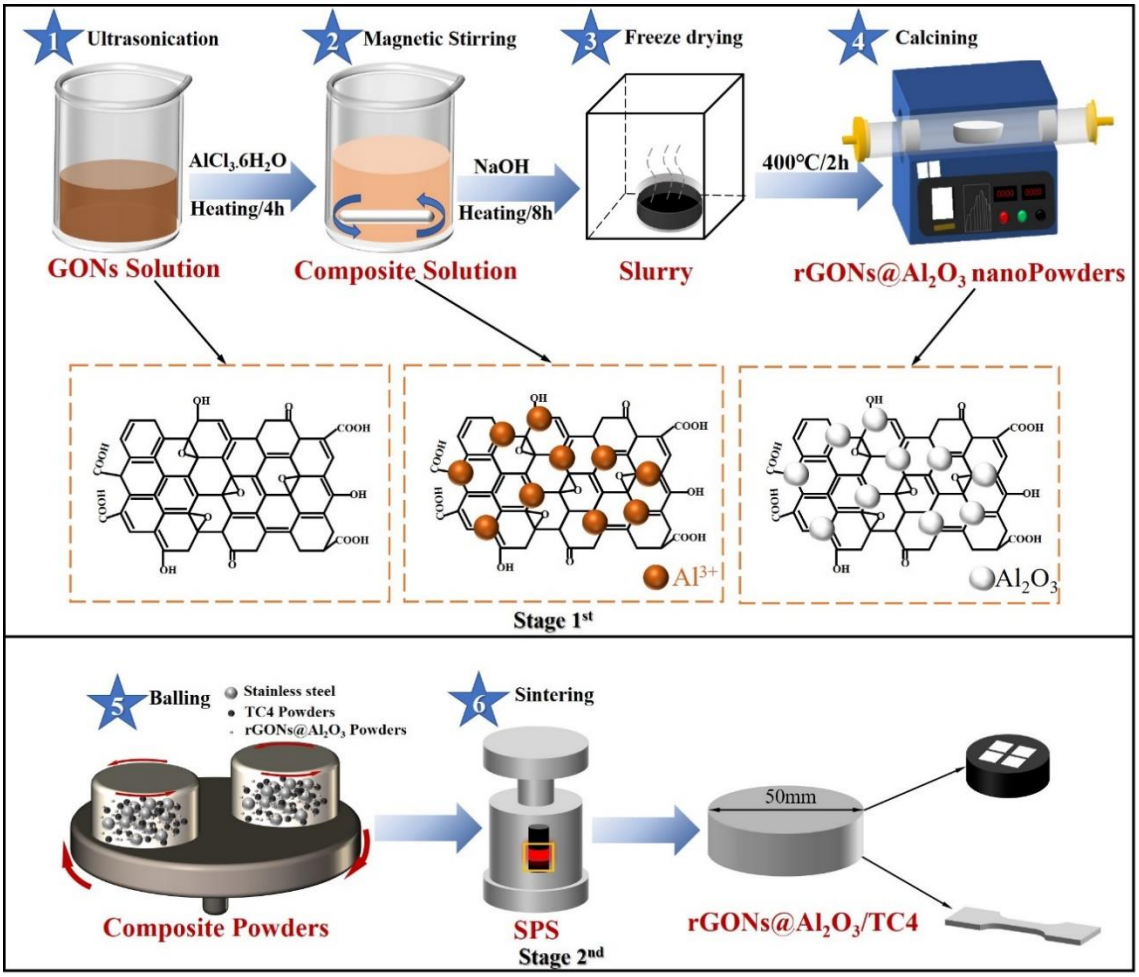

Figure 3. Schematic illustrations of the preparation of the rGONs@Al_2O_3 nanopowders and the rGONs@Al_2O_3/TC4 composites.

2.3 Characterization

Thermogravimetric analysis (TGA, DISCOVER DSC250) was performed for the as-obtained rGONs@Al_2O_3 powders to study their material contents. Crystalline phases of rGONs@Al_2O_3 nanopowders were characterized using an X-ray diffraction (XRD, BrukerAXS D4 Endeavor). Morphologies and microstructures of the rGONs@Al_2O_3 nanopowders and the rGONs@Al_2O_3/TC4 composites were characterized using a field emission SEM (FE-SEM, Zeiss GeminiSEM 500) and a transmission electron

microscope (TEM, Tecnai F30). To estimate the average grain size of the powders, we measured the values along different directions of each grain and obtained an average value from a large number of grains. The TEM sample was prepared by drop-casting the dispersions of the rGONs@Al_2O_3 onto a thin carbon film and then dried in air. X-ray photoelectron spectroscope (XPS, Thermo Fisher ESCALAB Xi+) was used to examine the formation of Al-O bond and the degree of reduction of GONs. Relative densities of the sintered rGONs@Al_2O_3/TC4 composites were examined using the Archimedes' method and the obtained results are listed in **Table 2**. The measured density of TC4 matrix (4.464g/cm^3) was found to be close to its theoretical density (4.510g/cm^3 ASTM B265) of the TC4 alloy, indicating that SPS process achieved a fully densified structure operated at a temperature of 1000 ^oC.

Tensile properties of sintered rGONs@Al_2O_3/TC4 composites were tested at room temperature using an MTS810 universal testing machine with a strain rate of 1 mm/min. Specimens for the tensile testing were cut into plate shape with a gauge length of 50 mm, a width of 13 mm and a thickness of 2 mm followed by a mechanically ground process. At least three tensile samples were tested to acquire an average value, and the fracture surface morphologies were analyzed using the SEM.

3. Result and discussion

3.1 Effect of co-precipitation temperature on morphology

Figure 3 shows morphologies of the rGONs@Al_2O_3 nanopowders prepared at different co-precipitation temperatures. Obviously, the color of the rGONs@Al_2O_3 precursor nanopowders was gradually changed from brown into black when the temperature was increased from 60 ^oC to 90 ^oC, indicating an increasing reduction trend of the graphene oxide in the rGONs@Al_2O_3 nanopowders [42], as shown in **Figures 4(a)~(c)**. The main reason of this trend is attributed to the temperature changes of the solutions during the co-precipitation process. Moreover, the sodium hydroxide acts as a reducing agent during the reaction [43], providing more nucleation sites for the adsorption of aluminum ions on the surfaces of rGONs nanosheets.

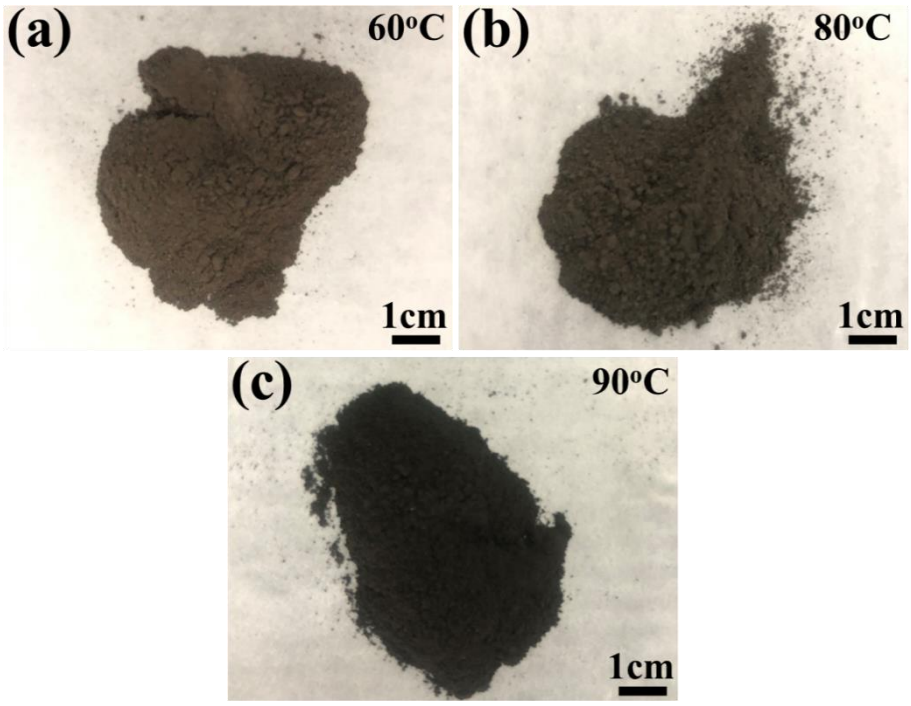

Figure 4. Macroscopic morphologies of the rGONs@Al_2O_3 precursor under different co-precipitation temperatures. (a) 60 ^oC; (b) 80 ^oC and (c) 90 ^oC, respectively.

Figure 5(a) shows the crystalline structures and compositions of the rGONs@Al_2O_3 nanopowders after the co-precipitation processes at different temperatures. The GONs appear to have a sharp peak at $2\theta = \sim 11^{\circ}$, corresponding to (001) crystallographic plane of GONs [44]. The weak peak around 43° is associated with the (100) plane of the hexagonal structure of carbon [45]. However, two new characteristic peaks located at $2\theta = 45.79^{\circ}$ and 67.30° were clearly observed in the 80-rGONs@Al_2O_3 and 90-rGONs@Al_2O_3 nanopowders (**Figure 5b**), which are corresponding to (400) and (441) crystal planes of γ-Al_2O_3 (PDF#04-0880). These results reveal that the Al_2O_3 nanoparticles and rGONs are co-existed in the rGONs@Al_2O_3 nanopowders. However, the diffraction peaks of GONs or rGONs were not detected in the rGONs@Al_2O_3 nanopowders as shown in **Figure 5.** This is mainly because these *in-situ* formed Al_2O_3 nanoparticles are covered onto the rGONs, which will inhibit the restacking of rGONs, keep the separated structures of the rGONs, and cause the disappearance of the diffraction peaks of GONs and rGONs [46]. Oxygen atoms in GONs play an important role as a bridge between carbon atom and metal atom, and it is quite easy to form strong metal-oxygen-carbon (such as Ag-O-C, Cu-O-C etc.) bonds in the preparation of rGONs@Al_2O_3 nanopowders, thus causing the strong interfacial adhesion between Al_2O_3 nanoparticles and rGONs [28, 47]. On the other hand, the interfacial reactions between Al_2O_3 and Ti can still occur owing to the Ti-Al_2O_3 reaction is thermodynamically favorable at different temperatures [48].

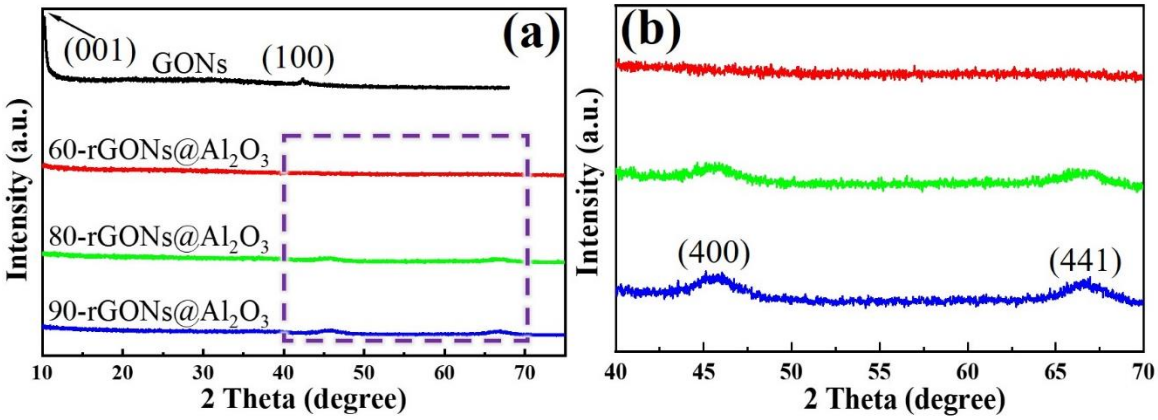

Figure 5. XRD patterns of (a) the rGONs@Al_2O_3 nanopowders fabricated at different co-precipitation temperatures; (b) enlarged XRD patterns at $2\theta = 40°\sim70°$ in Figure (a).

Figure 6 shows SEM images of the rGONs@Al_2O_3 nanopowders prepared at different co-precipitation temperatures. The morphologies of the rGONs@Al_2O_3 shown in **Figures 6(a)**, **(b)** and **(c)** demonstrate irregularly shaped three-dimensions blocks. When the co-precipitation temperatures is 60 ^oC, the high magnification image shown in **Figure 6(a_1)** reveals that the nanoscale Al_2O_3 (confirmed by TEM analysis in **Figure 7**) particles are homogeneously distributed on the surfaces of the rGONs fakes. However, with an increase of co-precipitation temperature, many aggregated Al_2O_3 particles and rGONs are clearly observed as shown in **Figures 6(b_1)** and **(c_1)**. It is worthwhile to mention that the amount of Al_2O_3 particles is decreased with the increase of co-precipitation temperature (e.g., comparing 80-rGONs@Al_2O_3 and 90-rGONs@Al_2O_3 nanopowders) as shown in **Figure 6d**. This is because the oxygen-containing functional groups of GONs are severely destroyed with the increase of co-precipitation temperature, which causes that the electrostatic adsorption between Al^{3+} and rGONs is weakened and a

large amount of bare aluminum hydroxide colloids are formed [43]. On the other hand, the bonding between aluminum ions and rGONs is weakened, and a large number of aluminum hydroxide colloids are removed during the centrifugation process [31].

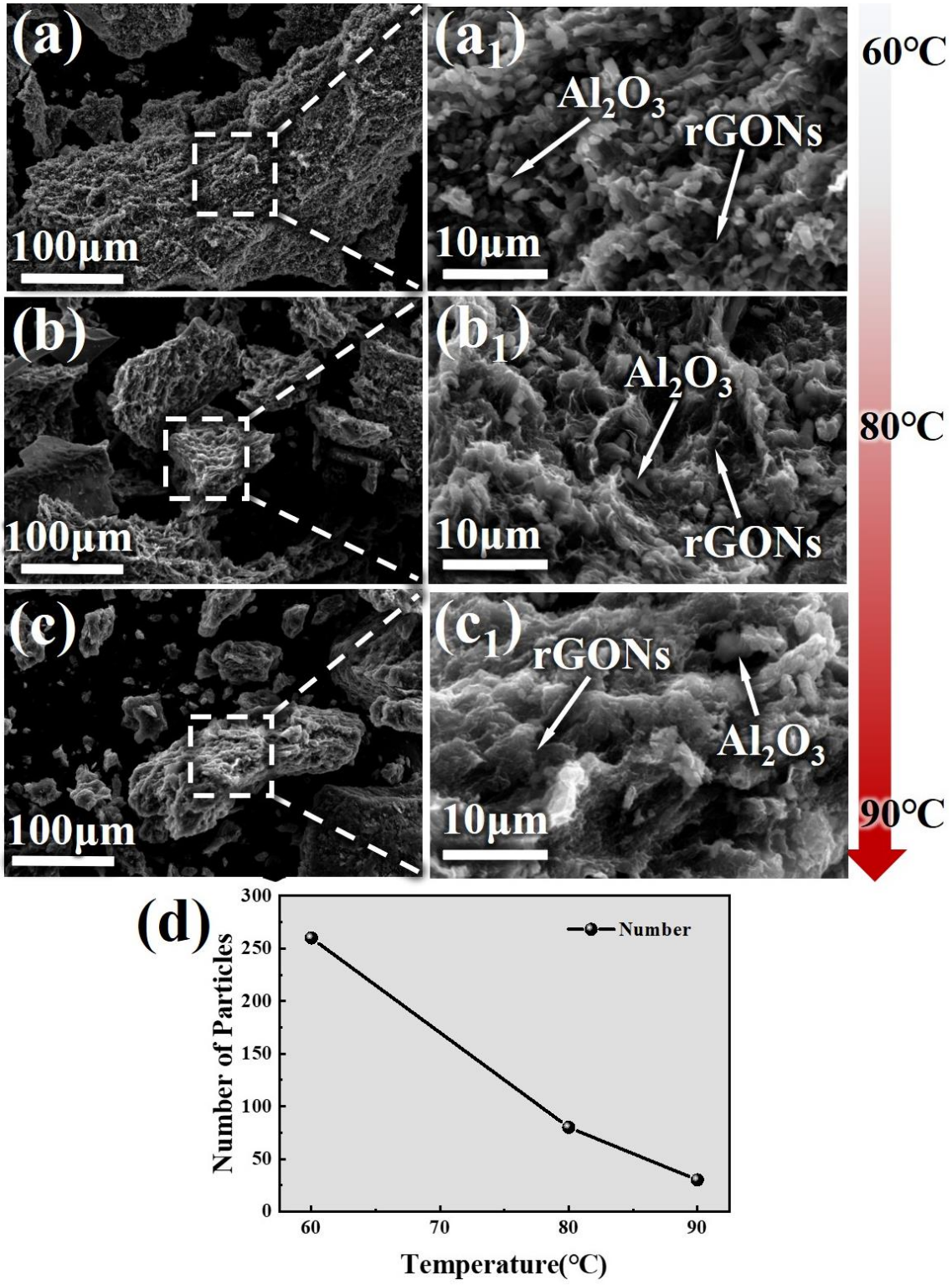

Figure 6. SEM images of rGONs@Al_2O_3 nanopowders under different co-precipitation temperatures. (a) 60 °C; (b) 80 °C and (c) 90 °C; (a_1), (b_1), and (c_1) are enlarged views of

the corresponding marked red regions in Figures 6(a), (b), (c), respectively; (d) the number of Al_2O_3 particles at the same multiple.

Figures 7(a) and **(b)** show the TEM images of the rGONs@Al_2O_3 nanopoweders, which reveal a transparent, rippled silk and wrinkled morphology. Moreover, the-particles with a diamond-like shape were uniformly distributed on the surfaces of the rGONs. To study the structure of the Al_2O_3 particles, the selected area electron diffraction image was taken from the surface of Al_2O_3 nanoparticles and the result is shown in **Figure 7c.** Planes of (-400), (-4-4-1) and (0-4-1) of γ-Al_2O_3 can be clearly seen. The high-angle annular dark-field--scanning transmission electron microscope (HADDF-STEM) morphology and EDS mapping images of rGONs@Al_2O_3 are shown in **Figures 7(d_1)~(d_3)**. Carbon elements are evenly distributed in the whole composite, whereas Al and O elements are more distributed on the white blocks, indicating that the rGONs are dispersed uniformly and the rGONs@Al_2O_3 nanopowders were synthesized successfully.

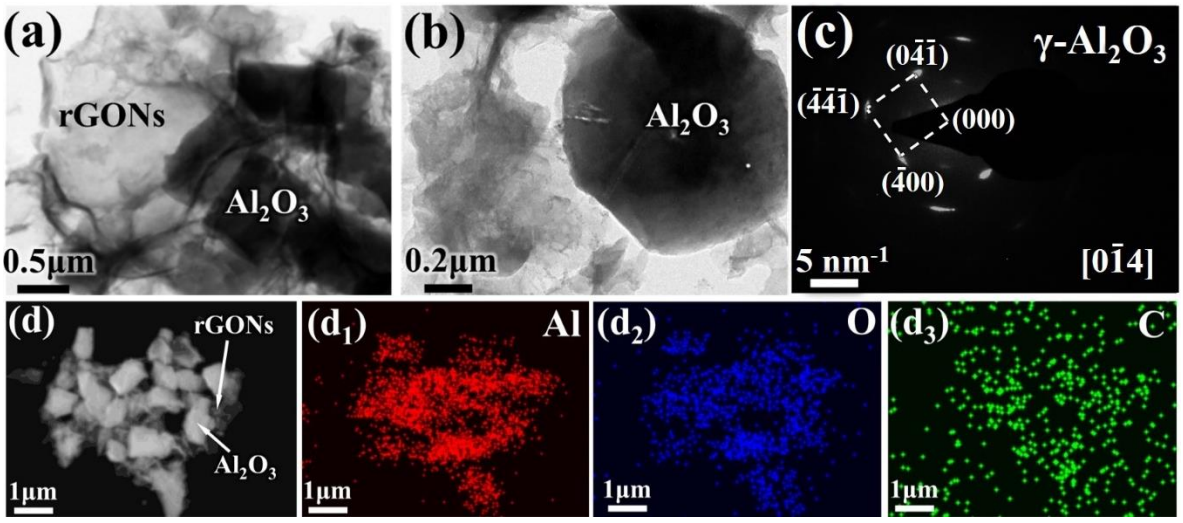

Figure 7. (a) and (b) Bright field TEM images of the rGONs@Al_2O_3 nanopowders; (c) the SAED pattern marked in Figure 7b. (d) High-angle annular dark-field-scanning transmission electron microscope image of the rGONs@Al_2O_3 nanopowders and (d_1)~(d_3) corresponding EDS mapping images of Figure 7d, respectively.

XPS data of the rGONs@Al_2O_3 nanopowders are shown in **Figure 8**. The main peaks in **Figure 8(a)** are located at 539.17 eV, 296.21 eV and 75.7 eV, which are corresponding to those of O1s, C1s and $Al2_P$ [28]. The existence of Na 1s weak peak is owing to the residual Na^+ ions (come from NaOH) in the solution that was not removed completely after the washing. The C1s spectra of the GONs and the rGONs@Al_2O_3 nanocomposites shown in **Figure 8(b)** can be divided into three main peaks, i.e. C–C at 284.5 eV, C–O at 286.2 eV, C=O at 287.8 eV [49]. The integral area occupied by the C-O bonds in the rGONs@Al_2O_3 nanomcoposite is obviously less than those of the GONs fakes, which indicates the removal of considerable number of functional-oxygen groups during the preparation process [39]. The C-O peak position of rGONs@Al_2O_3 nanocomposites is shifted to lower angle side slightly compared with that of GONs (**Figure 8b$_1$**) with an increase of co-precipitation temperatures, revealing that the formation of C-O-AlO structures [37, 50]. It should be also noted that the XPS spectrum of the rGONs@Al_2O_3 nanocomposite shows the peaks of Al-O at 75.7eV (**Figure 8c**), revealing that alumina nanoparticles are deposited on the surface of graphene.

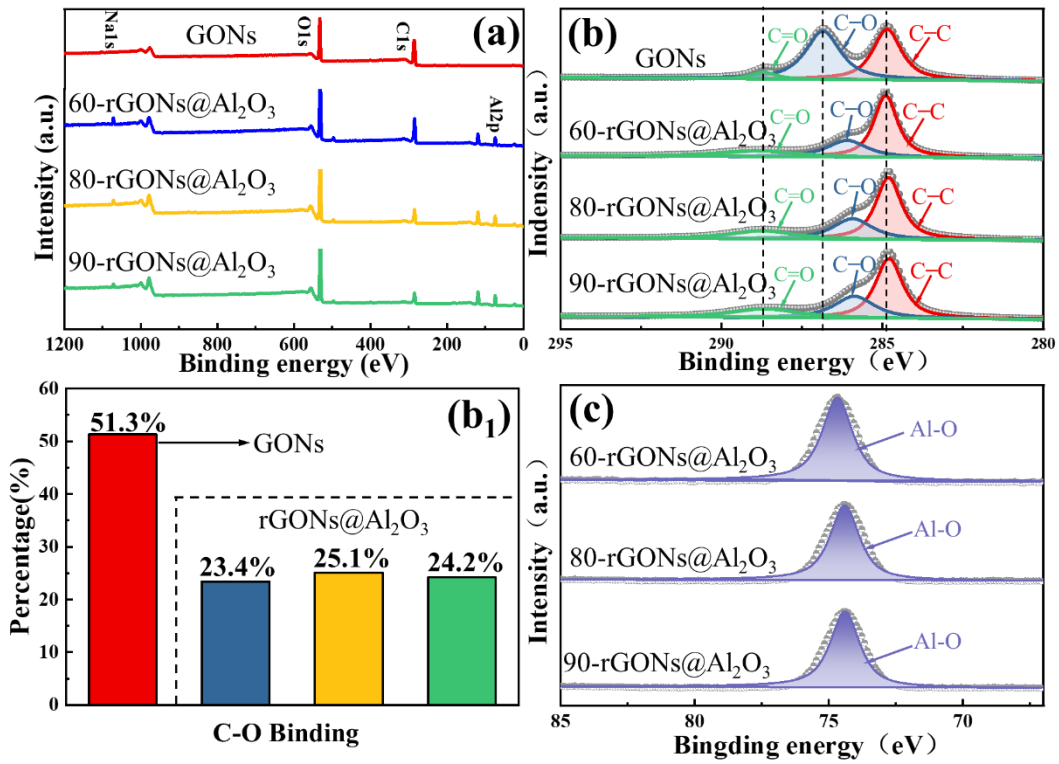

Figure 8. (a) XPS survey spectrum of the GONs and the rGONs@Al_2O_3; (b) The C1s XPS spectra of the GONs and the rGONs@Al_2O_3 nanocomposite powders; (b_1) the contents of C-O bonds in GONs and the rGONs@Al_2O_3 nanopowders; (c) The Al-O XPS spectra of the rGONs@Al_2O_3 nanocomposite powders, respectively.

3.2 Microstructure of the rGONs@Al_2O_3/TC4 composites

Figure 9 shows the SEM morphologies of the TC4 powders, the GONs/TC4 and the rGONs@Al_2O_3/TC4 composite powders, respectively. The TC4 powders in **Figure 9(a)** shows a nearly spherical shape with a wide distribution of the particle sizes, which is beneficial for the densification of the powders as the fine particles can fill the gaps in the triangle intersections of coarse particles during the SPS [16]. In **Figure 9(b_1)**, the GONs with their transparent and crumpled structures are absorbed on the surfaces of the TC4 powders. As seen in **Figures 9(c_1)** and **(d_2)**, the Al_2O_3 particles (confirmed by the EDS

mapping results in **Figures 9c2)** with an average size of ~ 1 μm are coated on the surfaces of TC4 powders, and the numbers of Al_2O_3 particles are increased with an increase of the rGONs@Al_2O_3 content. Moreover, the EDS analysis shown in **Figure 9(c2)** confirm that C elements are uniformly distributed on the whole surfaces of the TC4 powders, and rGONs in the rGONs/Al_2O_3 are embedded inside the TC4 particles. As compared with the SEM image of the rGONs/Al_2O_3 shown in **Figure 6**, those of the Al_2O_3 particles in **Figures 9(c)** and **(d)** show more irregular shapes and good dispersibility after ball milling, which is attributed to the plastic deformation, the fracture of the reinforcements, and the interaction with matrix powders during the ball milling process [18].

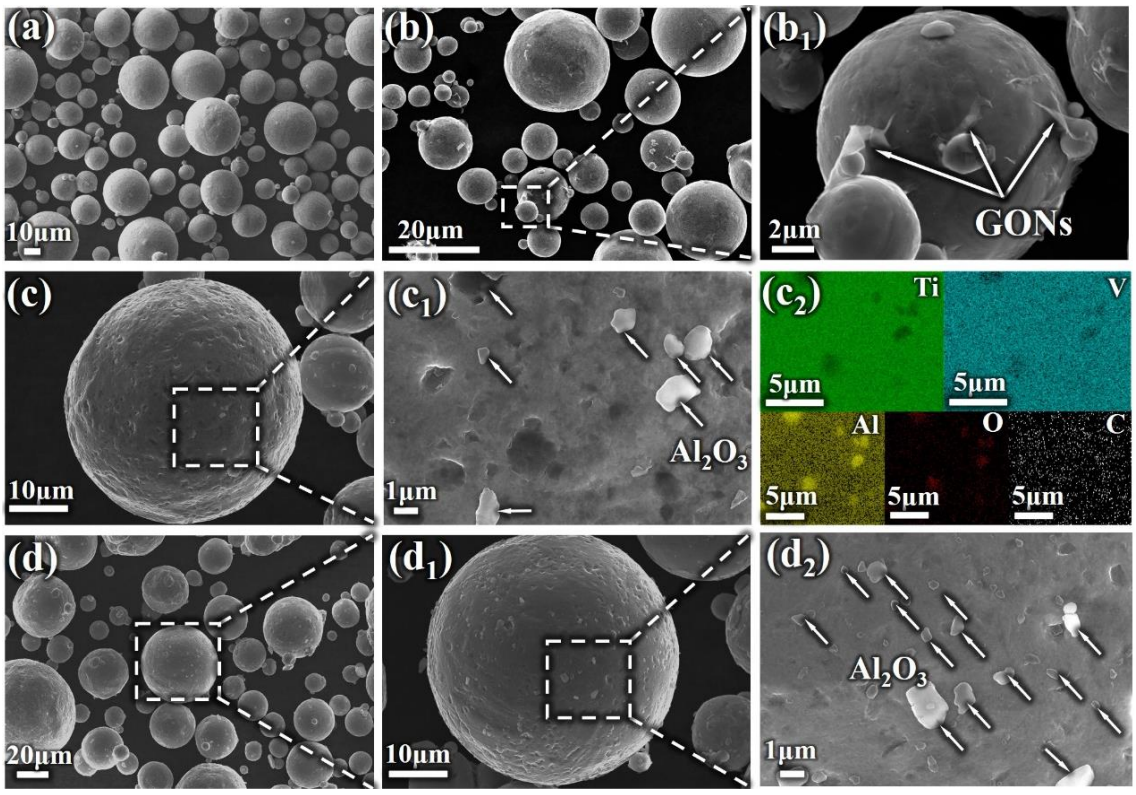

Figure 9. SEM images of (a) Raw TC4 powders, (b) 0.3rGONs/TC4 powders, (c) 0.3rGONs@Al_2O_3/TC4 powders, (d) 0.5rGONs@Al_2O_3/TC4, (b_1) and (c_1), (d_1) and (d_2)

are enlarged images of the corresponding marked regions in Figures 9(b) and (c), (d) and (d_1) respectively, (c_2) are elements distribution of Figure 9(c_1).

After sintered at 1000^{o}C, the primitive TC4 alloy (which has a typical Widmanstätten lamellar microstructure) is constituted of two phases (i.e. α+β phase), as shown in **Figure 10a**. The *in-situ* formed TiC phases (confirmed by EDS analysis in the inset of **Figure 10b**) are located at the grain boundaries in the 0.3rGONs/TC4 composite **(Figure 10b)**. For the rGONs@Al_2O_3/TC4 composite, the white particles with a small diameter are observed at the grain boundaries **(Figures 10c** and **d)**. The EDS data of point B in **Figure 10d₁** shows a higher content of Al, which confirms that the white particles are Al_2O_3 **(Figures 10c** and **d)**. Furthermore, **Figure 10e** shows that the average grain size of the 0.5rGONs@Al_2O_3 (101.62 μm) is smaller than that of TC4 matrix (121.62 μm), revealing that the addition of the rGONs@Al_2O_3 can effectively prevent the grain growth and refine the grains.

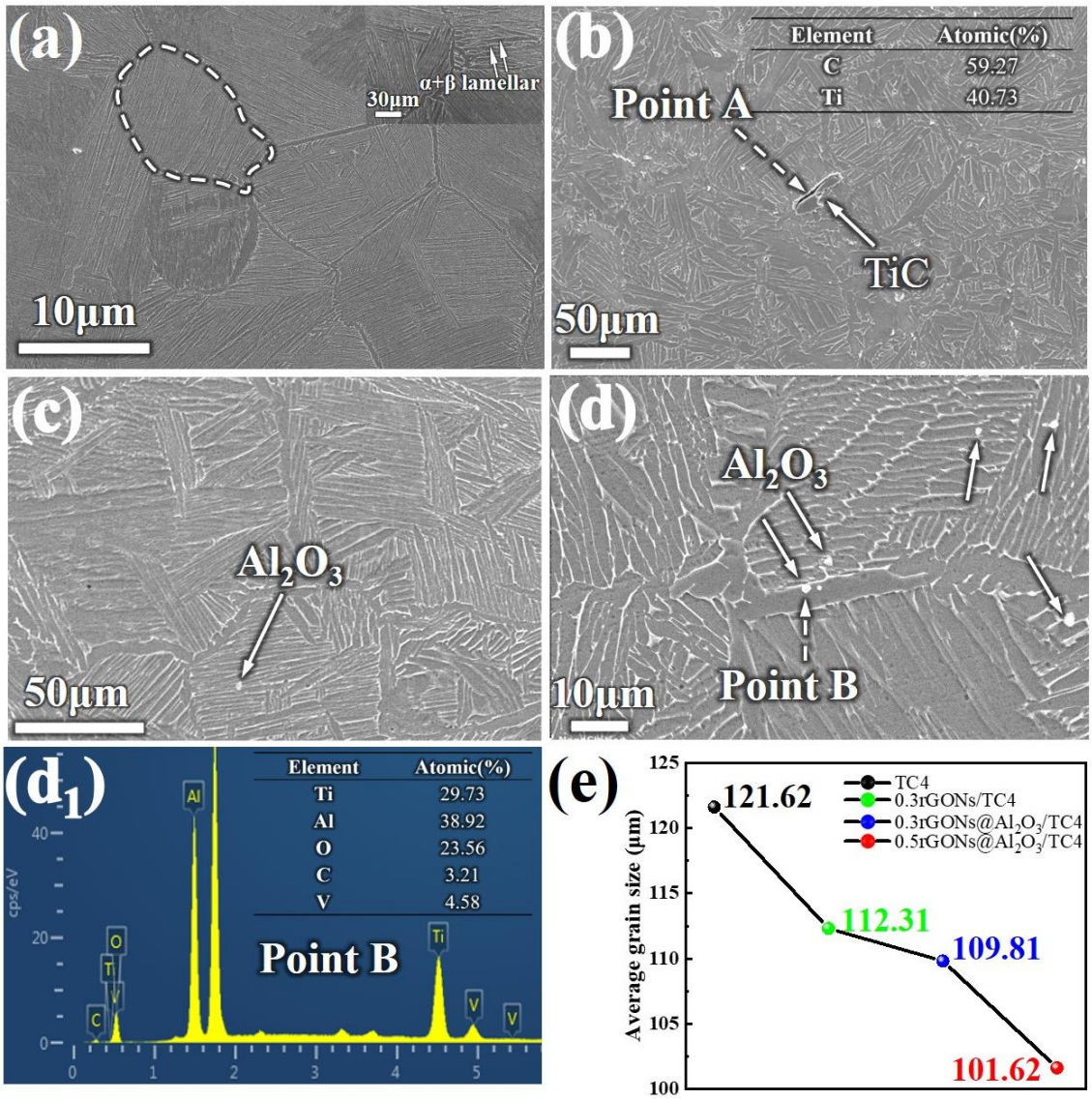

Figure 10. Microstructures of the TC4 matrix composite (a)TC4, (b) 0.3rGONs/TC4, (c) 0.3rGONs@Al_2O_3/TC4, (d) 0.5rGONs@Al_2O_3/TC4, (c_1) the EDS analysis of point A in(c), (e) the grain size of the TC4 composites, respectively.

3.3 Mechanical Properties and fracture mechanism of rGONs@Al_2O_3/TC4 composites

The tensile engineering stress-strain curves of the TC4 matrix composites reinforced with rGONs@Al_2O_3 are shown in **Figure 11**, and the corresponding mechanical properties are listed in **Table 2**. Compared with the curves in **Figure 11**, both the 0.2% yield strength (0.2% YS) and ultimate tensile strength (UTS) of the composites are increased with the addition of rGONs@Al_2O_3. For the as-sintered 0.5rGONs@Al_2O_3/TC4 composite, the 0.2% YS and UTS are ～950.5 MPa and 1022.5 MPa, respectively, which are 20.3% and 17% higher than those of the pure TC4 matrix (e.g., its 0.2% YS and UTS values are 789.2 MPa and 874 MPa, respectively).

The enhancement in the strength of the GONs@Al_2O_3/TC4 composites is caused by two main factors. Firstly, the well distributed reinforced rGONs@Al_2O_3, which have high stiffness and strength, acts as the efficient load-transfer medium in the Ti matrix. As described above, the rGONs@Al_2O_3 hybrids are uniformly distributed on the surface of the TC4 powders (**Figures 9c** and **d**) and boundaries of the metal matrix. This structure is beneficial for the dissipation of stress, and enhances the mechanical performance of the composites. Secondly, the rGONs@Al_2O_3 phases at the grain boundary play an important role in inhibiting the growth of TC4 matrix grain (**Figure 10e**). However, results show that the ductility of composites is decreased with an increasing of the rGONs@Al_2O_3 contents (see **Figure 11**). This is mainly attributed to the poor interfacial bonding between Al_2O_3 and Ti matrix, and the crack is mainly initiated at the Al_2O_3/TC4 interface (as discussed in **Figure 12**).

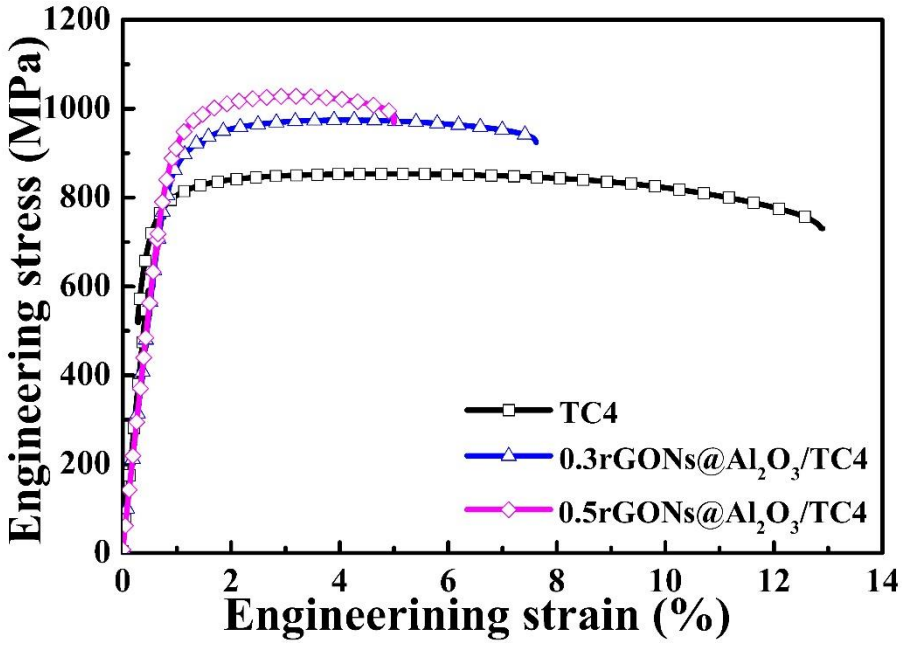

Figure 11. Engineering stress-strain curves of pure TC4, 0.3rGONs@Al_2O_3/TC4 and 0.5rGONs@Al_2O_3/TC4, respectively.

Table 2. Tensile properties and density of TC4 reinforced with GONs and rGONs@Al_2O_3 nanopowders, respectively.

Samples	YS (MPa)	UTS (MPa)	Elongation (%)	Measured density (g/cm^3)
TC4	789.18±6.37	873.97±7.48	12.2±1.5	4.464±0.0036
0.3rGONs@Al_2O_3/TC4	876.34±6.25	978.92±4.72	6.8±1.4	4.493±0.0052
0.5rGONs@Al_2O_3/TC4	950.69±8.32	1022.47±6.4	4.8±0.6	4.392±0.0928

Figure 12 shows SEM images of the fracture morphology of composites after tensile test. Numerous dimples and tearing ridges can be observed on the fracture surfaces of pure TC4 alloy as shown in **Figures 12(a)** and **(a_1)**, which reveals a typical ductile fracture mode. However, with the addition of the rGONs@Al_2O_3, the dimples are

dramatically decreased and cleavage steps are appeared in the fracture surfaces of the rGONs@Al_2O_3/TC4 composites. The cleavage steps become more obvious with the increase of rGONs@Al_2O_3 contents. Comparing **Figure 12(b)** and **Figure (c)**, the fracture mode of the composite is changed from a ductile fracture to a quasi-cleavage fracture due to the poor bonding interface between the ceramic and metal. **Figures 12(b_1)** and **(c_1)** show the fractured morphology of rGONs, revealing that the load can be effectively transferred from the TC4 matrix to rGONs during the tensile process. Furthermore, many trivial Al_2O_3 particles are observed in the dimples (**Figures 12b_1 and c_1**), which can resistant the movement of dislocations [51].

According to the above results, the strengthening mechanism of the rGONs@Al_2O_3/TC4 composites can be attributed to both fine grain hardening and effective load transfer. Particularly, Al_2O_3 particles can improve the uniform distributions of rGONs in titanium matrix and prevent the reaction between rGONs and titanium matrix. Hence, the loads can be effectively transferred from the TC4 matrix to rGONs and Al_2O_3 particles during the tensile process, owning to the good dispersion of rGONs and Al_2O_3 particles[52]. Al_2O_3 particles and rGONs are restricted at the grain boundary and resistant the dislocations' movement, thus significantly improving the strength of the matrix. However, the connectivity between TC4 matrix is easily broken due to the existence of particles, which is the main reason why the elongation is decreased sharply.

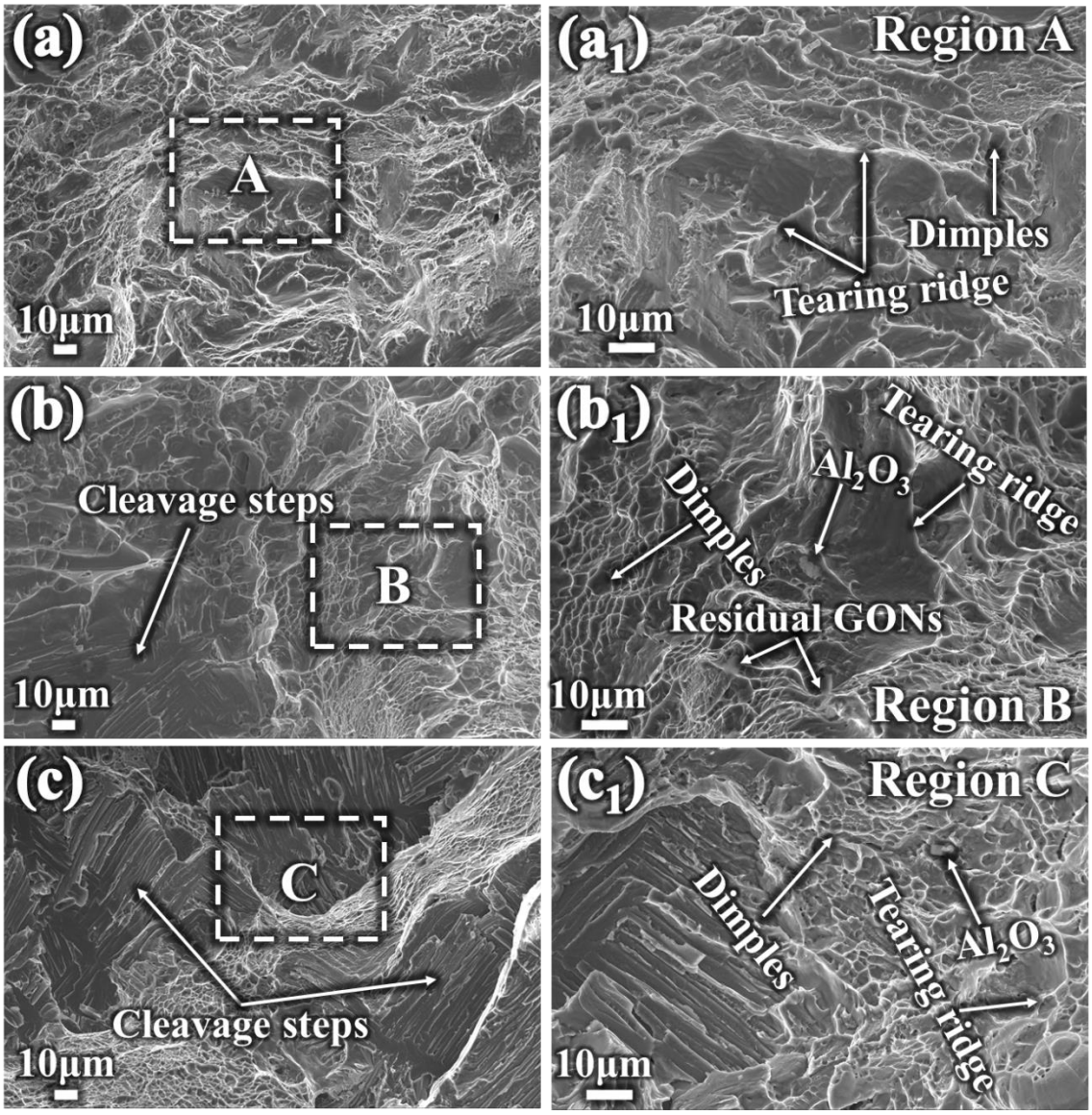

Figure 12. SEM fracture images (a) pure TC4, (b) 0.3rGONs@Al_2O_3/TC4 composite, (c) 0.5rGONs@Al_2O_3/TC4 composite, (a_1)～(c_1) enlarged images of corresponding marked red region in Figures 12(a), (b) and (c), respectively.

4. Conclusions

In summary, the rGONs@Al_2O_3/TC4 composites were successfully fabricated through processes of *in-situ* chemical co-precipitation, high temperature calcination, low-

energy ball milling and SPS. The γ-Al_2O_3 nanoparticles were uniformly wrapped with rGONs fakes, and the number of Al_2O_3 particles was decreased with the increase of co-precipitation temperature. The optimal synthesis conditions of the rGONs@Al_2O_3 nanopowders were found to be: co-precipitation stirred at 60°C and calcined at 400°C for 2h in a vacuum atmosphere. In particular, the average grain size of the rGONs@Al_2O_3 composites was smaller than that of TC4 matrix owing to the pinning effect of Al_2O_3 particles and GONs. In addition, the 0.5rGONs@Al_2O_3/TC4 composite showed 0.2% YS and UTS of～950.5 MPa and 1022.5 MPa, respectively, which are 20.3% and 17% higher than the pure TC4 matrix. The enhancements are mainly attributed to grain refinement and effectively load transfer. However, the ductility of the rGONs@Al_2O_3/TC4 composites was slightly decreased, which are attributed to the poor interfacial bonding between Al_2O_3 and matrix, and their fracture mode are a mixture of cleavage fracture and ductile fracture.

Declaration of competing interest

The authors declare that they have no known competing financial interests or personal relationships that could have appeared to influence the work reported in this paper.

Acknowledgements

This work was supported by the Shaanxi Science Foundation For Distinguished Young Scholars (2020JC-50), Key Research and Development Projects of Shaanxi

Province (No. 2019GY-164), Science and Technology Project of Weiyang District of Xi'an City (No. 201857), and UK Newton Mobility Grant (No. IE161019) and International Exchange Grant (IEC/NSFC/201078) through Royal Society and the National Natural Science Foundation of China, as well as Royal academy of Engineering UK-Research Exchange with China and India.

References

[1] Y. Hu, W. Cong, X. Wang, Y. Li, F. Ning, H. Wang, Laser deposition-additive manufacturing of TiB-Ti composites with novel three-dimensional quasi-continuous network microstructure: effects on strengthening and toughening, Composites Part B. 133 (2018) 91-100.

[2] C.N. Elias, D.J. Fernandes, F.M.D. Souza, E.D.S. Monteiro, R.S.D. Biasi, Mechanical and clinical properties of titanium and titanium-based alloys (Ti G2, Ti G4 cold worked nanostructured and Ti G5) for biomedical applications, Journal of Materials Research and Technology. 8 (2019) 1060-1069.

[3] J.W. Lu, Y.Q. Zhao, H.Z. Niu, Y.S. Zhang, Y.Z. Du, W. Zhang, W.T. Huo, Electrochemical corrosion behavior and elasticity properties of Ti–6Al–xFe alloys for biomedical applications, Materials Science & Engineering C. 62 (2016) 36-44.

[4] J.C. Williams, E.A. Starke, Progress in structural materials for aerospace systems, Acta Materialia. 51 (2013) 5775-5799.

[5] C.X. Lei, Y. Du, M. Zhu, W.T. Huo, Y.S. Zhang, Microstructure and mechanical properties of in situ TiC/Ti composites with a laminated structure synthesized by spark plasma sintering, Materials Science and Engineering A. 812 (2021) 141136.

[6] S.H. Xu, J.W. Qiu, H.B. Zhang, H.Z. Cao, Y. Liu, Friction behavior of Ti-30Fe composites strengthened by TiC particles, Transactions of Nonferrous Metals Society of China. 31(2021) 988-998.

[7] J.H. Yang, S.L. Xiao, Y.Y. Chen, L.J. Xu, X.P. Wang, J.Tian, D.D. Zhang, Z.Z. Zheng, Microstructure evolution during forging deformation of (TiB+TiC+Y_2O_3)/α-Ti composite: DRX and globularization behavior, Journal of Alloy and Compounds. 827 (2020) 154170.

[8] C. Han, L.Y. Cang, L.X. Liang, L.P. Chen, N. Zhao, X.K. Zhu, Effect of composition and sintering temperature on mechanical properties of ZrO_2 particulate-reinforced titanium-matrix composite, Transactions of Nonferrous Metals Society of China. 22 (2012) 1855-1859.

[9] S. Shi, S. Cho, T. Goto, T. Sekino, The effects of sintering temperature on mechanical and and electrical properties of Al_2O_3/Ti composites, Materials Today Communications. 25 (2020) 101522.

[10] X. Shen, Z. Zhang, S. Wei, F. Wang, S. Lee, Microstructures and mechanical properties of the in situ TiB–Ti metal–matrix composites synthesized by spark plasma sintering process, Journal of Alloy and Compounds. 509 (2011) 7692-7696.

[11] K. Geim, K.S. Novoselov, The rise of graphene, Nature Materials 6 (2007) 183-191.

[12] C. Lee, X.D. Wei, J.W. Kysar, J. Hone, Measurement of the elastic properties and intrinsic strength of monolayer graphene, Science. 321(2008) 385-388.

[13] A.H. Castro, F. Neto, N. Guinea, N.M.R. Peres, The electronic properties of graphene, Reviews of Modern Physics. 81 (2009) 4710-4764

[14] L.L. Dong, J.W. Lu, Y.Q. Fu, W.T. Huo, Y. Liu, D.D. Li, Carbonaceous nanomaterial reinforced Ti-6Al-4V matrix composites: properties, interfacial structures and strengthening mechanisms, Carbon. 164 (2020) 272-286.

[15] Q. Yan, B. Chen, L. Cao, K.X. Liu, S. Li, L. Jia, K. Kondoh, J.S. Li, Improved mechanical properties in titanium matrix composites reinforced with quasi-continuously networked graphene nanosheets and in-situ formed carbides, Journal of Materials Science & Technology. 96 (2022) 85-93.

[16] N. Tian, L.L. Dong, H.L. Wang, Y.Q. Fu, W.T. Huo, Y. Liu, J.S. Yu, Y.S. Zhang, Microstructure and tribological properties of titanium matrix nanocomposites through powder metallurgy using graphene oxide nanosheets enhanced copper powders and spark plasma sintering, Journal of Alloy and Compounds. 867 (2021) 159093.

[17] W.G. Chen, T. Yang, L.L. Dong, A. Elmasry, J.L. Song, N. Deng, A. Elmarakbi, T. Li, H.B. Lv, Y.Q. Fu, Advances in graphene reinforced metal matrix nanocomposites: Mechanisms, processing, modelling, properties and applications, Nanotechnology and Precision Engineering. 3 (2020) 189-210.

[18] Y. Zhou, L.L. Dong, Q.Y. Yang, W.T. Huo, Y.Q. Fu, J.Y. Yu, Y. Li, Y.S. Zhang, Controlled Interfacial Reactions and Superior Mechanical Properties of High Energy Ball Milled/Spark Plasma Sintered Ti–6Al–4V–Graphene Composite, Advanced Engineering Materials 23 (2021) 2001411.

[19] B. Zhang, F.M. Zhang, F. Saba, C.Y. Shang, Graphene-TiC hybrid reinforced titanium matrix composites with 3D network architecture: Fabrication, microstructure and mechanical properties, Journal of Alloy and Compounds. 859 (2021) 15777.

[20] L.L. Dong, B. Xiao, Y. Liu, Y.L. Li, Y.Q. Fu, Y.Q. Zhao, Y.S. Zhang, Sintering effect on microstructural evolution and mechanical properties of spark plasma sintered Ti matrix composites reinforced by reduced graphene oxides, Ceramics International. 44 (15) (2018) 1783-17844.

[21] L. Zan, G.L. Fan, Z.Q. Tan, Z.Q. Li, Q. Guo, D.B. Xiong, D. Zhang, A versatile method for uniform dispersion of nanocarbons in metal matrix based on electrostatic interactions, Nano-Micro Letters. 8 (2016) 54-64.

[22] F.M. Zhang, J. Wang, T.F. Liu, C.Y. Shang, Enhanced mechanical properties of few-layer graphene reinforced titanium alloy matrix nanocomposites with a network architecture, Materials & Design. 186 (2020) 108330.

[23] L.L. Dong, B. Xiao, L.H. Jin, J.W. Lu, Y. Liu, Y.Q. Fu, Y.Q. Zhao, G.H. Wu, Y.S. Zhang, Mechanisms of simultaneously enhanced strength and ductility of titanium matrix composites reinforced with nanosheets of graphene oxides, Ceramics International. 45 (2019) 19370–19379.

[24] J.S. Yu, Y.Q. Zhao, S. X. Huang, Y.Q. Zhao. J.W. Lu, L.L. Dong, Enhanced mechanical and tribological properties of graphene nanoplates reinforced TC21 composites using spark plasma sintering. Journal of Alloy and Compounds. 873 (2021) 159764.

[25] Y. Song, W. Chen, W.W. Liu, W.L. Li, Y.G. Wang, D. Zhao, X.B. Liu, Microscopic mechanical properties of titanium composites containing multi-layer graphene nanofillers, Materials & design. 109 (2016) 256-263.

[26] C.Y. Shang, F.M. Zhang, B. Zhang, F. Chen, Interface microstructure and strengthening mechanisms of multilayer graphene reinforced titanium alloy matrix nanocomposites with network architectures, Materials & design. 196 (2020) 109119.

[27] J.W. Lu, L.L. Dong, Y. Liu, Y.Q. Fu, W. Zhang, Y. Du, Y.S. Zhang, Y.Q. Zhao, Simultaneously enhancing the strength and ductility in titanium matrix composites via discontinuous network structure, Composites Part A. 136 (2020) 105971.

[28] H. B. Luo, Y.W. Sui, J.Q. Qi, Q.K. Meng, F.X. Wei, Y.Z. He, Mechanical enhancement of copper matrix composites with homogeneously dispersed graphene modified by silver nanoparticles, Journal of Alloy and Compounds. 729 (2017) 293-302.

[29] L.L. Dong, Y.C. Ding, W.T. Huo, W. Zhang, J.W. Lu, L.H. Jin, Y.Q. Zhao, G.H. Wu, Y.S. Zhang, A green and facile synthesis for rGO/Ag nanocomposites using one-step chemical co-reduction route at ambient temperature and combined first principles theoretical analyze, Ultrasonics- Sonochemistry. 53 (2019) 152-163.

[30] V. Botcha, Divakar, D.S. Sutar, S.S. Major, Study of GO-Cu_2O and RGO-Cu nanocomposite monolayer sheets prepared by modified Langmuir Blodgett route, The Journal of Physics and Chemistry of Solids. 118 (2018) 158-165.

[31] G. Goncalves, P.A.A.P. Marques, G.M. Granadeiro, H.L. Singh, Surface modification of graphene nanosheets with gold nanoparticles: The role of oxygen moieties at graphene surface on gold nucleation and growth, Chemistry of Materials. 21 (2009) 4796-4802.

[32] N.T. Li, S.C. Tang, X.K. Meng, Preparation of Pt-GO composites with high-number-density Pt nanoparticles dispersed uniformly on GO nanosheets, Progress in Natural Science: Materials International. 26 (2016) 139-144.

[33] X.N. Mu, H.N. Cai, H.M. Zhang, Q.B. Fan, F.C. Wang, Z.H. Zhang, Y.X. Ge, R. Shi, Y. Wu, Z. Wang, D.D. Wang, S. Chang, Uniform dispersion and interface analysis of nickel coated graphene nanoflakes/ pure titanium matrix composites, Carbon. 137 (2018) 146-155.

[34] A.M. Jastrzebska, J. Karcza, R. Letmanowski, D. Zabost, E. Ciecierska, J. Zdunek, E. Karwowska, M. Siekierski, A. Olszyna, A. Kunicki, Synthesis of the RGO/Al_2O_3 core–shell

nanocomposite flakes and characterization of their unique electrostatic properties using zeta potential measurements, Applied Surface Science. 362 (2016) 577-594.

[35] L.L. Dong, Y.Q. Fu, Y. Liu, J.W. Lu, W. Zhang, W.T. Huo, L.H. Jin, Y.S. Zhang. Interface engineering of graphene/copper matrix composites decorated with tungsten carbide for enhanced physico-mechanical properties, Carbon. 173 (2021) 41-53.

[36] L.L. Dong, W. Zhang, Y.Q. Fu, J.W. Lu, X.T. Liu, N. Tian, Y.S. Zhang, Reduced graphene oxide nanosheets decorated with copper and silver nanoparticles for achieving superior strength and ductility in titanium composites, ACS Applied Materials Interfaces. 13 (2021) 43197−43208.

[37] K. Fu, X. Zhang, C.S. Shi, E.N. Zuo, F. He, J.J. Liu, N.Q. Zhao, C.N. He. An approach for fabricating Ni@graphene reinforced nickel matrix composites with enhanced mechanical properties. Mat. Sci. Eng. A 715(7) 2018 108-116.

[38] R. Guan, Y. Wang, S. Zheng, N. Su, Z. Ji, Z. Liu, Y. An, B. Chen. Fabrication of aluminum matrix composites reinforced with Ni-coated graphene nanosheets. Mat. Sci. Eng. A 754(29) (2019) 437-447.

[39] C. J. Shuai, B. Wang, S.Z. Bin, S.P. Peng, C.D. Gao, Interfacial strengthening by reduced graphene oxide coated with MgO in biodegradable Mg composites, Materials & design. 191 (2020), 108612.

[40] W.L. Zhang, H.J. Choi, Y.K Leong, Facile fabrication of graphene oxide-wrapped alumina particles and their electrorheological characteristics, Materials Chemistry & Physics. 145 (2014) 151-155.

[41] L. Zhao, R. Wang, S.J. Wu, Z.P. Xue, D.M. Zhu, J.X. Zou, X.L. Li, In situ observation of metal ion interactions with graphene oxide layers: from the growth of metal hydroxides to metal oxide formation, Carbon. 184 (2021) 721-727.

[42] J.Y. Cho, J.I. Jiang, W.K. Lee, S.Y. Jeong, J.Y. Hwang, H.S. Lee, J.H. Park, J.H. Park, S.Y. Jeong, H.J. Jeong, H.J. Jeong, G. Lee, J.T Han, Fabrication of high-quality or highly porous graphene sheets from exfoliated graphene oxide via reactions in alkaline solutions, Carbon. 138 (2018) 219-226.

[43] X.B. Fan, W.H. Peng, Y. Li, X.Y. Li, S.L. Wang, G.L. Zhang, F.B. Zhang, Deoxygenation of exfoliated graphite oxide under alkaline conditions: A green route to graphene preparation, Advanced Materials. 20 (2008) 4490-4493.

[44] L.L. Dong, W.G. Chen, N. Deng, C.H. Zheng, A novel fabrication of graphene by chemical reaction with a green reductant, Chemical Engineering Journal. 306 (2016) 754-762.

[45] J.J. Niu, J.N. Wang, Activated carbon nanotubes-supported catalyst in fuel cells, Electrochim Acta. 53 (2008) 8058–8063.

[46] Z.W. Yang, Y.Z. Wan, G.Y. Xiong, D.Y. Li, Q.P. Li, C.Y. Ma, R.S. Guo, H.L. Luo, Facile synthesis of $ZnFe_2O_4$/reduced graphene oxide nanohybrids for enhanced microwave absorption properties, Materials Research Bulletin. 61 (2015) 292-297.

[47] K.T. Kim, S.I. Cha, T. Gemming, J. Eckert, S.H. Hong. The role of interfacial oxygen atoms in the enhanced mechanical properties of carbon-nanotube reinforced metal matrix nanocomposites. Small. 4 (2008) 1936-1940.

[48] S.F. Shi, S.H. Cho, T. Goto, T. Sekino. The effects of sintering temperature on mechanical and electrical properties of Al_2O_3/Ti composites. Materials Today Communications 25(2020) 101522.

[49] H.W. Tien, L.Y. Huang, S.Y. Yang, J.Y. Wang, C.C. M. Ma, The production of graphene nanosheets decorated with silver nanoparticles for use in transparent, conductive films, Carbon. 49 (2011) 1550-1560.

[50] C.T. Chiu, Y.J. Teng, B.H. Dai, L.Y. Tsao, W.C. Lin, K.W. Wang, L.C. Hsu, C.T. Li, H.T.T. Nguyen, C.Y. Chiang, W.H. Huang, Novel high-entropy ceramic/carbon composite materials for the decomposition of organic pollutants, Materials Chemistry and Physic. 275 (2022) 125274.

[51] R.Casati, M.Vedani, Metal matrix composites reinforced by nano-particles—a review, Metals. 4 (2014) 65–83.

[52] S.E. Shin, H.J. Choi, J.Y. Hwang, D.H. Bae, Strengthening behavior of carbon/metal nanocomposites, Scientific Reports. 5 (2015) 16114.